Atomic structure of different surface terminations of polycrystalline ZnPd

M. Lowe, A. Al-Mahboob, D. Ivarsson, M. Armbrüster, J. Ardini, G. Held, F. Maccherozzi, A. Bayer, V. Fournée, J. Ledieu, et al.

Atomic structure of different surface terminations of polycrystalline ZnPd

M. Lowe,[1] A. Al-Mahboob,[1,2] D. Ivarsson,[3] M. Armbrüster,[3] J. Ardini,[4] G. Held,[4,5] F. Maccherozzi,[5] A. Bayer,[6] V. Fournée,[7] J. Ledieu,[7] J. T. Sadowski,[2] R. McGrath,[1] and H. R. Sharma[1]

[1]*Surface Science Research Centre, Department of Physics, University of Liverpool, Liverpool L69 3BX, United Kingdom*

[2]*Center for Functional Nanomaterials, Brookhaven National Laboratory, P.O. Box 5000, Upton, New York, USA*

[3]*Faculty of Natural Sciences, Institute of Chemistry, Materials for Innovative Energy Concepts, Chemnitz University of Technology, 09107 Chemnitz, Germany*

[4]*Department of Chemistry, University of Reading, Reading, Berkshire, RG6 6AF, United Kingdom*

[5]*Diamond Light Source, Harwell Science and Innovation Campus, Didcot, OX11 0DE, United Kingdom*

[6]*Department of Chemistry and Pharmacy, Friedrich Alexander Universität Erlangen-Nürnberg, Nikolaus-Fiebiger-Str. 10 91058 Erlangen, Germany*

[7]*Institut Jean Lamour, CNRS-Université de Lorraine, Campus Artem 2 allée André Guinier BP 50840 54011 Nancy Cedex, France*

(Dated: September 24, 2024)

Abstract

The intermetallic compound ZnPd has been found to have desirable characteristics as a catalyst for the steam reforming of methanol. The understanding of the surface structure of ZnPd is important to optimize its catalytic behavior. However, due to a lack of bulk single-crystal samples and the complexity of characterizing surface properties in the available polycrystalline samples using common experimental techniques, all previous surface science studies of this compound have been performed on surface alloy samples formed through thin film deposition. In this study, we present findings on the chemical and atomic structure of the surfaces of bulk polycrystalline ZnPd studied by a variety of complementary experimental techniques, including, scanning tunneling microscopy (STM), X-ray photoelectron spectroscopy (XPS), low energy electron microscopy (LEEM), photoemission electron microscopy (PEEM) and microspot low energy electron diffraction (μ-LEED). These experimental techniques, combined with density functional theory (DFT)-based thermodynamic calculations of surface free energy and detachment kinetics at the step edges, confirm that surfaces terminated by atomic layers composed of both Zn and Pd atoms are more stable than those terminated by only Zn or Pd layers. DFT calculations also demonstrate that the primary contribution to the tunneling current arises from Pd atoms, in agreement with the STM results. The formation of intermetallics at surfaces may contribute to the superior catalyst properties of ZnPd over Zn or Pd elemental counterparts.

I. INTRODUCTION

Methanol steam reforming (MSR) is a promising route to provide clean hydrogen for fuel cells in mobile high-density energy applications [1]. A number of different catalysts have been proposed for MSR [1–5]. Among them is the intermetallic compound (IMC) ZnPd. Despite higher costs compared to the Cu-based systems, ZnPd possesses industrial potential as it shows MSR at millisecond contact time, high conversion, and low temperature compared to other catalysts [6, 7]. In addition, ZnPd supported on ZnO is also a hydrogenation catalyst [1], catalyses the steam reforming of ethanol [8], and can be used as a catalyst to grow ZnO nanorods [9].

MSR produces CO_2 and CO in addition to hydrogen, and the suppression of CO remains the greatest challenge [1]. The presence of CO in traces of > 20 ppm in hydrogen has to

be avoided to enable the long-time performance of proton exchange membrane (PEM) fuel cells to generate electricity without a further cleaning step [10, 11].

Most research so far has been devoted to $Cu/ZnO/Al_2O_3$ catalysts for MSR. Cu-based catalysts are efficient and selective toward CO_2, generating CO levels of around 1500 ppm in MSR [12–14]. However, the applied Cu-based catalysts are pyrophoric materials, and metal sintering results in a rapid degradation of the catalytic activity. ZnPd/ZnO catalysts have been shown to compete with Cu-based catalysts [15] and have set benchmarks of about 1000 ppm CO [1]. If Pd is dispersed on a ZnO support the catalyst possesses the required CO_2 selectivity and maintains a high efficiency and thermal stability [16]. The selectivity has been attributed to the combined action of ZnPd and ZnO [17], and more recently the involvement of the oxidic support by a Mars-van Krevelen mechanism could be shown for In_xPd_y/In_2O_3 [18].

There is huge industrial potential and demand for future energy applications. However, most surface science studies have been carried out on thermodynamically unstable ZnPd thin films [19] and no information about the surface atomic structure of bulk samples have been reported yet. This is because most surface science experimental techniques require large single crystalline samples. Despite the immense efforts, attempts to synthesize ZnPd single crystals have failed so far. Therefore, the polycrystalline sample presented in this study represents the best approach to a 'single crystal' currently available. Our work opens the opportunity to determine the direction-dependent catalytic properties under relevant conditions, as soon as single crystals become available. A reactor specifically designed for this purpose has been developed and validated [20]. A comprehensive understanding of the surfaces of ZnPd would be an important step in the further understanding and development of ZnPd catalysts.

Most samples of ZnPd used for model studies under ultra-high vacuum (UHV) conditions have been grown as a surface alloy by depositing Zn on low-index Pd surfaces. The ZnPd surface alloy is often only several atomic layers thick. The surface alloy has been characterized as being a corrugated surface. Zn atoms sit 0.25 Å higher than Pd when a ZnPd film is formed on Pd(111), while Pd atoms sit 0.06 Å higher than Zn on the Pd(110) substrate [21, 22]. On the Pd(111) surface, which has been most heavily studied, the surface consists of alternating Zn and Pd atomic rows, in a three-domain p(2×1) structure [23]. The Pd-Zn bond is stronger than both the Pd-Pd bond and the Zn-Zn bond and also creates the

ordered, perturbed rows on the surface [24, 25].

The intermetallic compound ZnPd displays a lower density of states near the Fermi level compared to Pd, and this is important as CO selectivity is believed to be directly related to the density of states around the Fermi level. Tsai *et al.* [26] and Nozawa *et al.* [27] studied the relationship between catalytic activity and the valence electron density of states of isostructural ZnPd, ZnPt, and ZnNi. ZnPd was found to be more catalytically selective than isostructural ZnPt and ZnNi, which decomposes under reaction conditions [28]. ZnPd has a valence electron density of states similar to elemental Cu, whereas the other two compounds have a different valence band structure, suggesting that selectivity is directly related to the density of states near the Fermi level. Equally the Zn:Pd ratio at the surface and subsurface is a key determinant for electronic properties, as long-range effects from subsurface layers control the electronic structure and hence influence catalytic properties [29, 30].

The study of polycrystalline samples using common laboratory techniques is very challenging, and such studies are rarely reported. In this work, we examine the structure of the surfaces of differently oriented grains of polycrystalline ZnPd by a number of state-of-the-art surface characterization techniques complemented by density functional theory (DFT) calculations. The surface atomic structure is studied by scanning tunneling microscopy (STM) and microspot low energy electron diffraction (μ-LEED). The surface chemical structure is probed by X-ray photoelectron spectroscopy (XPS). This has been supplemented with studies of surface morphology by low energy electron microscopy/photoemission electron microscopy (LEEM/PEEM), which allows for spectroscopic, microscopic, and diffraction analyses of individual grains in the polycrystalline sample. Our study demonstrates that a polycrystalline sample is suitable for investigating the relative stability of surfaces.

II. METHODS

A. Experimental Details

A polycrystalline foil of ZnPd was synthesized by vapor-solid reaction as described in reference [31] using Pd foil (ChemPur, 99.9%) and zinc granules (ChemPur, 99.999%) separated by a neck in an evacuated quartz-glass ampoule. The ampoule was located upright

(Zn at the bottom) in an oven and heated with 1 K/min to 450 °C, held for 24 hours, and further heated to 900 °C with 1 K/minute. At this temperature, the sample was annealed for two months to ensure homogeneity. The sample composition was verified by determining the mass gain of the sample and determined to be $Zn_{50.96(1)}Pd_{49.04(1)}$. Metallographic characterization revealed a polycrystalline single-phase sample showing the typical twinning for this synthesis route [32].

The polycrystalline sample was then polished using successively finer grades of diamond paste (6 μm, 1 μm and 0.25 μm), before being cleaned ultrasonically in methanol. The sample was then mounted in a UHV chamber (base pressure 10^{-10} mbar) and surfaces were prepared by Ar^+ ion sputtering followed by annealing at varying temperatures from 150 °C to 350 °C for 30-60 minutes. An initial sputtering time of 85 minutes was used to remove contaminants due to long air exposure, and the lengthy polishing procedure. Temperatures were measured using a K-type thermocouple on the manipulator heating stage. Several sputter-anneal cycles were needed to obtain a clean surface. The surface atomic and chemical structures were then characterized by STM and XPS. The STM was operated in constant current mode with a positive bias voltage of 0.8-1.2 V with a tunneling current of 0.1 nA. Therefore, the provided STM images correspond to the unoccupied states of ZnPd.

To get an overview of domain orientation and crystallites, LEEM and PEEM were employed. Surface termination was determined by selected area micro-beam LEED (μ-LEED) recorded in LEEM.

B. Computational Procedures

The DMol^3 package is employed in the commercial DFT Electronic Structure Program, Biovia Materials Studio [33, 34], to calculate kinetic stability and thermodynamic energies. DFTD (Generalized Gradient Approximation (GGA) + dispersion correction) calculations were carried out using the GGA functional within the Perdew-Burke-Ernzerhof (PBE) framework [35] and the dispersion correction method of Grimme [36]. The relativistic corrections [37, 38] were employed using DSPP (DFT-Semicore Pseudopotential) [39]. See the Supplementary Materials for details.

STM simulation was done using the CASTEP module. Prior to the STM simulation, geometry optimization was performed again using the functional in DMol^3. The functional

chosen for the geometry optimization in this stage was identical to the one used in CASTEP for the STM simulation. The geometry of the surface and sub-surface was optimized, constraining the surface unit cell parameters as reported in the literature, with an additional six to eight atomic layers underneath. Calculations were done using a revised Perdew-Burke-Ernzerhof (PBE) [35] GGA functional, RPBE [40], and relativistic correction using the VPSR pseudopotential [41]. The Double Numerical plus polarization (DNP) basis set version 4.4 [42] was used in the calculations. The simulated STM images presented in the report correspond to the unoccupied states of ZnPd at 0.8 eV.

ZnPd realizes the CuTi type of structure ($P4/mmm$, Zn on Wykoff site $1a$ (0 0 0) and Pd on $1d$ (0.5 0.5 0.5)) with $a = 2.8931(1)$ Å and $c = 3.3426(2)$ Å [27]. In this report, we describe the surfaces in terms of the tetragonal notation.

III. RESULTS AND DISCUSSION

A. Grain structure of the sample

The clean surface was prepared *in situ* and examined by LEEM-mirror imaging, PEEM, and selected area μ-LEED patterns. Figure 1(a, b) shows LEEM and PEEM images taken from the same area of the sample. LEEM visualizes the domain structure (crystallites) of ZnPd where the domain-contrast is energy-dependent and associated with a small relative tilt of the facet normal to the surface average and a work-function difference related to the chemical/structural composition of the surface. The contrast in PEEM is associated with the work-function of the surfaces of individual domains.

For some crystallites, the incident beam in LEEM could not be set perfectly perpendicular because of its polycrystalline nature. Therefore, the contrast does not reflect the true crystallographic orientation of the crystallites. However, LEEM images are adequate to determine the size of the crystallites. The spread of grain sizes is in a range of approximately 2 - 20 μm. PEEM images clearly show three contrasts: light (L), gray (G), and dark (D) as presented in Figure 1(b), suggesting that the crystallites predominantly have three surface orientations. PEEM images show additional contrast (brightest) at domain boundaries. This contrast could be linked to carbon segregation at these boundaries during annealing. However, the quantity of carbon present was insufficient to appear in the XPS spectrum.

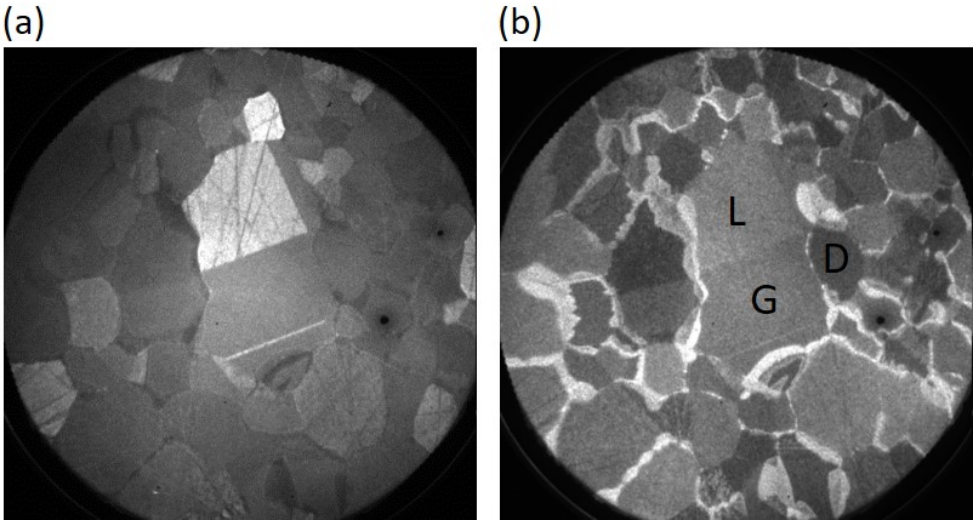

FIG. 1. (a) LEEM (mirror) and (b) PEEM images taken from the same area of the sample (50 μm $\times$ 50 μm). The surface was prepared by sputtering followed by annealing at 240 °C for 30 min and then at 220 °C overnight. Three contrasts are observed in PEEM: light (L), gray (G), and dark (D). We measured μ-LEED patterns from each representative grain (Figure 5).

As the bulk does not contain any carbon, the source of the segregated carbon could be the diamond paste used for polishing the surface. We confirm the existence of the three surface orientations of the grains by scanning the surface using μ-LEED (refer to Section III D).

B. Surface Chemical Structure Studied by XPS

The surface chemical composition after different sample treatments was examined by XPS. XPS was first used to characterize the sample as-loaded into the chamber. The surface was then cleaned by sputter-annealing until no contaminant was detected on the surface. Figure 2 shows XPS spectra from the surface after each treatment (air-exposed, sputtered, and sputter-annealed). We also measured XPS spectra following the sputtering of the previously sputter-annealed sample to check reproducibility. The core level (Pd 3d, Zn 3d, Zn 2p) and Auger Zn LMN peak positions determined from XPS spectra are shown in Table I. Here, we also provide the elemental core levels from previous reports for comparison. The composition of the near-surface region after sputtering and annealing is shown in Table II. For these analyses, XPS peaks were fitted using a Shirley background and a mixture of Gaussian-Lorentzian convoluted lineshapes and Doniach-Sunjic lineshapes for asymmetrical

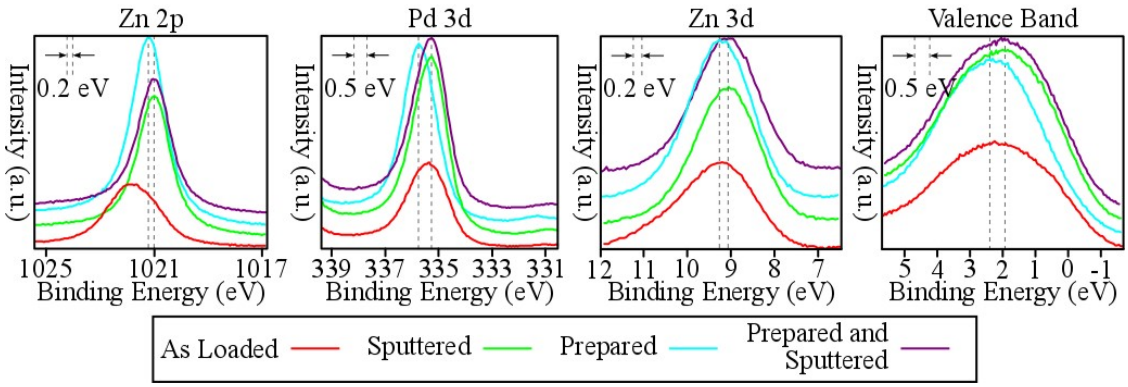

FIG. 2. XPS spectra for Pd $3d$, Zn $2p$, Zn $3d$ and valence band after the surface was subjected to different treatments: air exposed (as loaded), sputtered, sputter-annealed (prepared) and sputtered the prepared surface. The same shifts to higher binding energy of 0.2 eV in Zn species and 0.5 eV in Pd species are present after sputtering regardless of the initial condition of the surface.

peaks.

The surface of the air-exposed sample is heavily contaminated by O- and C-species. The Zn $2p$ core level from the air-exposed surface is shifted to a higher binding energy indicating the formation of ZnO.

Composition analysis suggests a preferential sputtering of the Zn in the surface (Table II), as expected; elements of the lightest weight and lower surface energy are susceptible to preferential sputtering [43]. There is also a large difference between elemental Pd and Zn surface energies, estimated to be 1.92 Jm^{-2} and 0.99 Jm^{-2}, respectively [1].

The preferential sputtering of Zn leads to elemental Pd on the surface. This is evidenced by the core level shifts of the Pd $3d$ core level. The Pd $3d$ core level after sputtering is similar to that of elemental but shifted to lower binding energy by 0.5 eV compared to ZnPd. The surface recovers the bulk composition after annealing. Both Zn and Pd core levels display the expected characteristics for the intermetallic compound as described in the literature [44], including characteristic binding energy shifts (Table I).

Elemental Zn has a high vapor pressure in UHV, and when annealed would sublimate and contaminate the UHV chamber. However, Zn in ZnPd did not show such behavior due to the lower chemical potential of Zn in the compound [49]. To test the possible evaporation of Zn, we placed a mass spectrometer detector directly in front of the sample (within 30 mm) and annealed the sample up to 510 °C. No Zn was observed in the mass spectrometer

Element/ Transition	Air Exposed Surface	Sputtered Surface	Prepared Sample	Element	IMC
Pd $3d$	335.7 eV	335.0 eV	335.9 eV	335.0 eV [45]	336.2 eV [44]
Zn $2p$	1021.9	1020.8 eV	1021.3 eV	1021.8 eV [46]	
Zn $3d$	9.2 eV	9.0 eV	9.3 eV	10.0 eV [47]	9.2-9.6 eV [44]
Zn LMM	992.5 eV	993.2 eV	992.7 eV	992.1 eV [48]	992.0 eV [44]

TABLE I. Comparison of binding energies for core levels and kinetic energies for Auger peaks from XPS data given in Figure 2. Uncertainties estimated at 0.1 - 0.2 eV. Core levels and Auger peak energies from previous reports are also presented for comparison in columns 5 and 6.

Preparation State	Zn (at%)	Pd (at%)
Sputtered	38.6	61.4
Annealed	50.5	49.5

TABLE II. Change in atomic concentration, as measured by XPS, of the surface of ZnPd following cleaning cycles. The uncertainty is estimated at 5 at% for all values.

spectra during the annealing processes, which verifies the stability of surface Zn up to this temperature. This indicates a significant difference to ZnPd surface alloys in which Zn evaporates at this temperature as reported by Gabasch *et al.* [50].

C. Surface Atomic Structure Studied by STM and DFT

The surface prepared by sputtering and annealing was found to be very rough in STM and contained large regions of highly-stepped terraces across the majority of the surface. In areas where it was possible to find atomically flat terraces, these were limited to no more than approximately 30 nm $\times$ 30 nm in size.

Independent of the underlying grain orientation, we observed only (110), (101), (111) and (114) surfaces. The surface orientations were identified by comparing STM images with the structure model of each of these surfaces (Figure 3). The unit cells in the model and STM, which are marked in Figure 3, match each other, indicating bulk-like termination of

	STM			LEED			Model			Surface Energy
Surface	a	b	θ	a	b	θ	a	b	θ	(eV Å^{-2})
(110)	-	4.1	-			90°	3.3	4.2	90°	0.0697
(101)	4.2	2.7	90°	3.4	4.1	-	4.4	2.9	90°	0.0662
(111)	4.4	4.6	53°	4.4	4.7	54°	4.1	4.4	55°	0.0802
(114)	4.1	8.0	90°	-	-	-	4.1	8.8	90°	0.0832

TABLE III. Comparison of lattice parameters, a, b (in Å) and θ, determined from STM presented in Figures 3 and 4 and μ-LEED patterns presented in Figure 5, together with surface energy of each orientation calculated by DFT.

the different surfaces. Simulated STM images by DFT and μ-LEED results (Section III D) also confirm the formation of these surfaces. Surface lattice parameters extracted from STM and μ-LEED are compared with that of the bulk model in Table III.

The most commonly observed surface in STM was (101). The (111) surface is much less prevalent than the (101) surface but is capable of forming large (relative to the other surfaces) terraces as can be seen in Figure 3(d). The (110) and (114) surfaces are observed in a highly-stepped area of the surface (see Figure 3(e-f)). The (114) surface still provides atomic resolution, while the (110) surface does not exhibit terraces large enough to analyze and display atomic resolution. However, we could identify this surface from the facet angle in STM. This surface makes a facet with the (114) surface at an angle of 113.9°, which is close to the expected angle between the (114) and (110) planes (112.2°).

Zn atoms are either not detected or less well-resolved in STM. To demonstrate this, we compare experimental STM images with the model structure and DFT simulated STM images of the bulk terminated (101) and (111) surfaces in Figure 4. Both the experimental data and the simulation for this surface show clear protrusions at the Pd sites, while the less-resolved striped patterns are related to the Zn atoms. It is likely that the stripes are also contributed to by Pd atoms from the second layer. Since the second layer Pd atoms are slightly offset from the top layer Zn, the stripes in STM appear to be slightly misaligned with the DFT results.

The (111) surface contains both Zn and Pd atoms, with the Pd and Zn atoms separated by an interplanar distance of 0.9 Å. The density of states at the Pd sites dominates over

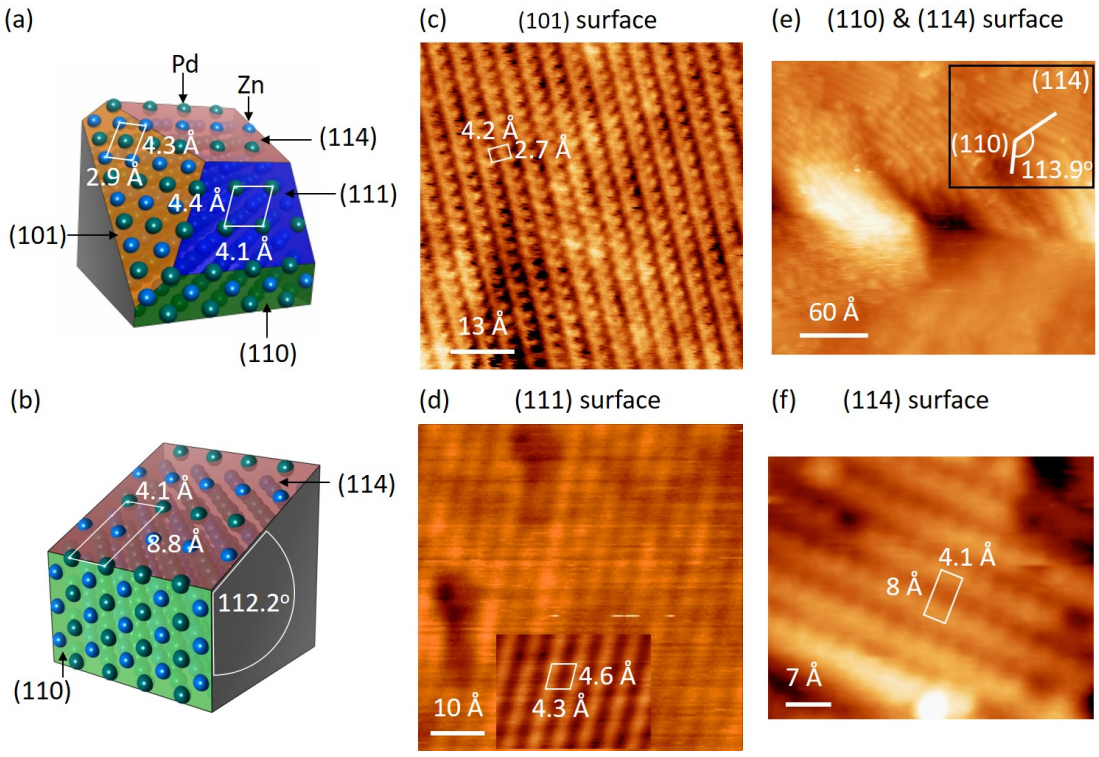

FIG. 3. (a-b) Schematic models of all surfaces observed by STM from the ZnPd polycrystalline sample. (c) STM image of (101) surface. Image is presented after merging with FFT filtered image. (d) STM image of (111) surface. Inset is a FFT filtered image. (e) STM image of the region of the surface displaying highly-stepped terraces. Rectangle marks an area where we identified (110) and (114) facets with a 113.9° angle between them. (f) STM image of the (114) surface. Unit cells are marked in the models and STM images.

those at the Zn sites, suggesting that the brighter spots observed in STM images are related to Pd atoms. The lack of Zn in the STM images was previously reported by Weirum *et al.* in their studies on surface alloys [51]. The local density of states calculation suggests that the Fermi level has contributions arising predominantly from Pd $4d$ derived states [52]. Therefore, Pd atoms are expected to appear significantly brighter than Zn atoms in STM for the bias voltages used in this experiment.

D. Surface Orientation of Crystallites Identified by μ-LEED

As discussed in Section III A, the surface was mapped by LEEM after sputter-annealing. Once the surface map was created, it was possible to measure μ-LEED patterns from in-

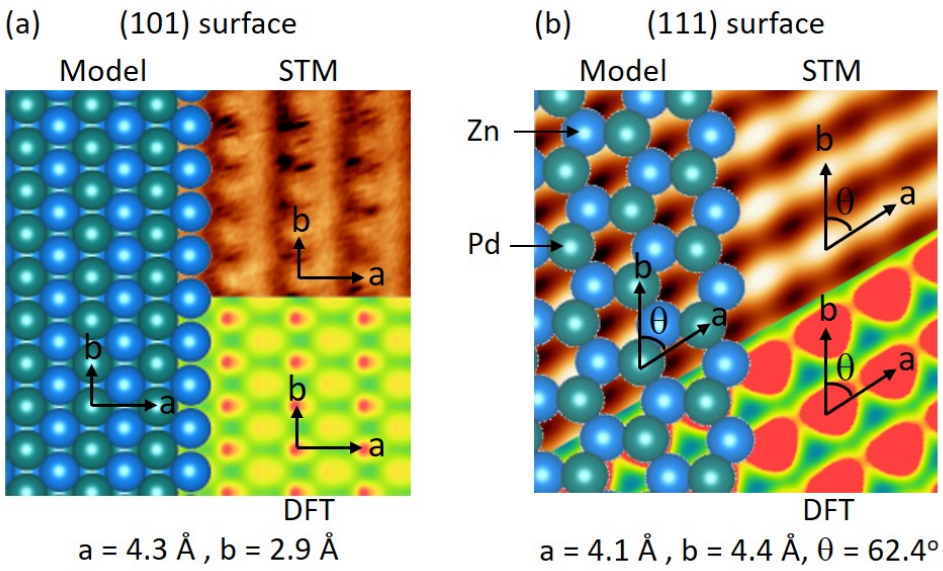

FIG. 4. Comparison of STM results to model structure and simulated STM data of (101) (a) and (111) (b) surfaces of ZnPd. Unit cell vectors are marked. The corresponding lattice parameters are presented in Table III. For the (101) surface, in both the experimental data and the simulation clear protrusions can be observed at Pd atoms, while the striped patterns are related to Zn atoms. In the (111) surface, bright spots correspond to Pd atoms. The lattice parameters provided at the bottom are derived from the model. Both experimental and simulated STM images correspond to the unoccupied states of ZnPd.

dividual grains. Figure 5 shows μ-LEED patterns taken from gray, light, and dark grains of LEEM in Figure 1(b). By comparing these patterns with the reciprocal lattices of the surfaces, we could identify the surface orientation of these grains to be (101), (111), and (114).

The lattice parameters calculated from the μ-LEED patterns are in good agreement with the model, suggesting the surfaces correspond to bulk truncation (see Table III). The lattice vectors were calculated by scaling each pattern to a Si(111) 7×7 μ-LEED pattern taken at the same energy. The lack of movement of diffraction spots in LEEM meant that once the window was scaled at the same energy, patterns of different incident electron energies could be compared directly to the Si pattern. It was then possible to average out the effect of distortions or difficulty in finding the center of diffuse spots.

We note that the LEED pattern assigned to the (114) surface shows long-range order

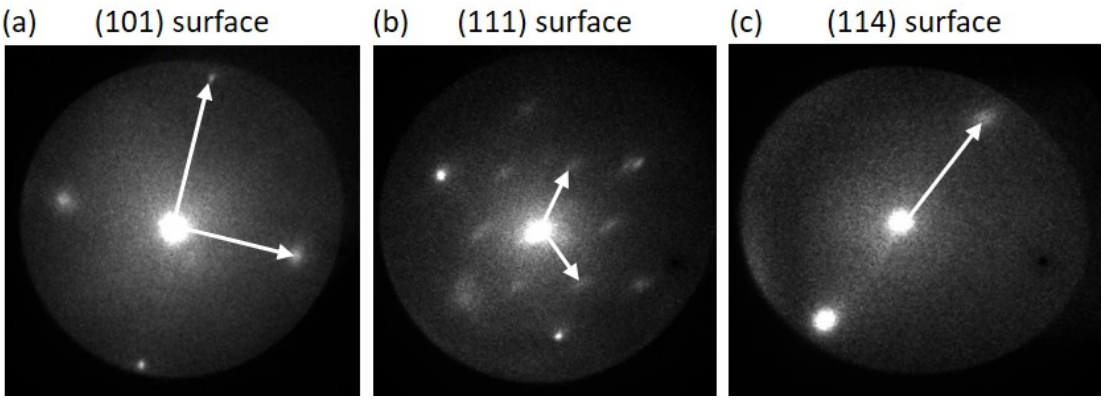

FIG. 5. μ-LEED patterns taken from gray, light, and dark grains in LEEM (Figure 1(b)). Representative grains are marked in Figure 1(b). LEED patterns confirm the surface orientation of (101) (a), (111) (b), and (114) (c). Unit cell vectors are marked. The lattice parameters determined from μ-LEED patterns are given in Table III. Beam energies for (a), (b), and (c) patterns are 16, 12, and 12 eV, respectively.

along one direction. For the given beam energy of 12 eV, the first-order Bragg diffraction along the other high-symmetry direction of the (114) surface is outside the reciprocal space range imaged in LEEM. However, we were also unable to detect spots along this direction, even at higher beam energies. This is likely due to the domain size along this direction being smaller than the transfer width for reciprocal space imaging in LEEM (a few tens of nanometers). Additionally, the atomic ordering along this direction is poorer compared to the perpendicular direction. This observation is supported by the STM images shown in Figure 3 (f).

E. Stability of Surfaces Studied by DFT

To understand the relative stability of the surfaces, we studied the Wulff constructions of the ZnPd crystal at various temperatures by DFT-based thermodynamics computations. The Wulff construction (Figure 6 (a)) represents an equilibrium shape of the crystal for a given temperature obtained by minimizing the total surface free energy of the interface between the crystal and vacuum. Corresponding thermodynamic free energies are plotted in Figure 6 (b). The plots show that, at the temperatures used to prepare the surface, the only favored surface structures are (101) and (110) (Figure 6 (a)). These surfaces are among

those observed experimentally.

We plot the surface free energy for different crystal orientations at various temperatures in Figure 6 (b). The surface energy at 0 K in the plot corresponds to the binding energy of surface atoms per unit surface area relative to the identical number of atoms placed in the vacuum slab when no thermodynamic component (vibration entropy) is considered (DFT surface energy). That is, surface energy is defined here as the difference in energy for the formation of a surface relative to a crystal having no surface, and the formation energy of free atoms relative to the crystal. Surface energy is determined from the differences in total DFT energies between the atomistic models having identical numbers of atoms. The surface free energy at temperatures higher than 0 K in the plot represents the sum of DFT surface energy plus vibration-free energies of surface atoms (see supplementary information for details). The (101) and (110) surfaces exhibit the lowest and second lowest surface free energies across all temperatures. Therefore, these surfaces are stable kinetically and thermodynamically.

To understand the kinetic process further, we studied the detachment kinetics at the step edges (refer to the supplementary materials for calculation details). The calculated decay probability of different surfaces as a function of annealing temperatures is shown in Figure 6 (c). With increasing temperature, the (111) and (114) surfaces decay slower, while the (101) and (110) surfaces decay faster. That means if the kinetic processes prevail over thermodynamic processes, the (101) and (110) surfaces would vanish after these treatments. However, these surfaces, being thermodynamically favored, would regrow at high temperatures. Due to these two competitive processes for surface stability, it is expected that too many cycles or too high temperatures would produce a surface with facets along these possible crystallographic orientations such that the surface would be extremely rough and unsuitable for imaging by STM. Optical microscope images of the surface after extensive sputter-anneal treatments also confirm the faceting of the surface (image not shown here). To further explore this phenomenon, we annealed the sample at 220 °C for 12 hours. The annealing turned the mirror-like shiny surface to hazy appearing rough to the naked eye, suggesting the faceting and roughening of the crystal upon annealing.

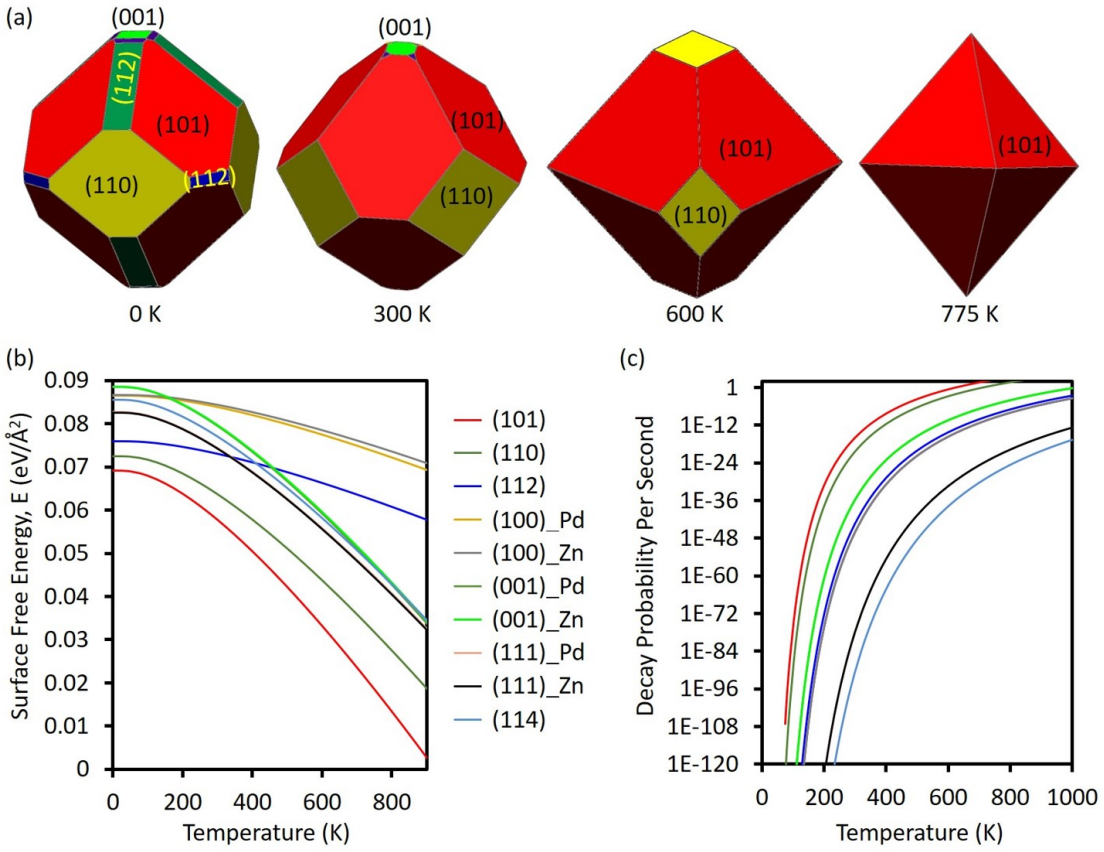

FIG. 6. (a) Wulff constructions of the ZnPd crystal at different temperatures (indicated below the plots) calculated by DFT-based thermodynamics calculations. Different colors represent facets of different orientations. (b) Surface free energy as a function of temperature for various surfaces. (c) Kinetically limited decay probability of different surfaces as a function of temperature. In this plot, only kinetically limited detachments are considered. No thermodynamic competition is accounted for in the plots.

F. Discussion

All the observed surfaces are constructed from Zn and Pd, as can be seen in the top and side view of each surface plane displayed in Figure 7. This can be understood by reference to previous observations that the heteroatomic interaction is stronger than the homoatomic ones in the crystal [24, 25]. Even the Pd terminated (111) surface is constructed from both elements, as the Zn sits only slightly lower than the Pd in the structure (approximately 0.9 Å). The (001) surface was not observed experimentally. Although the decay probability of this surface is intermediate (Figure 6(c)), it might not be formed at the initial growth

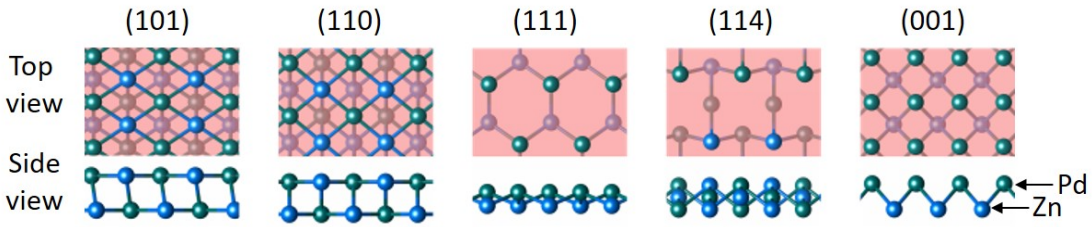

FIG. 7. Schematic of various surfaces of ZnPd. The (110), (101), (111), and (114) surfaces are observed by STM and contain both Zn and Pd atoms in or near to the top surface layer. The (001) surface, which has not been observed, has single-element termination.

temperature as it is thermodynamically unfavored. This surface is the only fully single-element terminated surface, among the high-symmetry surfaces. The non-observation of the (001) surface thus supports our argument that Zn-Pd interactions are essential to stabilize the surface. The conclusions also corroborate the idea that the catalytically active Pd metal sites are stabilized at the surface of PdZn due to the bonding network.

The presence of intermetallics on surfaces could lead to ZnPd demonstrating improved catalyst characteristics. This argument is supported by previous works reported by the authors [1], but also by other research groups. For example, ZnPd shows enhanced catalytic properties in methanol steam reforming [3], the selective hydrogenation of acetylene in the gas-phase [53], and phenylacetylene in the liquid phase [54], the electrochemical CO_2 reduction reaction [55], the oxygen reduction reaction [56], the ethanol oxidation reaction [57], and the nitrogen oxidation reaction [58].

IV. CONCLUSION

A preparation procedure has been developed to enable structural studies on the atomic scale on polycrystalline ZnPd bulk samples. The sample was checked with XPS to confirm the intermetallic nature of the surface and the chemical cleanliness of the sample. Following this, STM and μ-LEED studies were performed to understand the surface termination tendencies of the crystal. STM and LEED identify (110), (101), (111), and (114) surfaces. The stability of these surfaces is confirmed by DFT-based thermodynamic calculations of surface free energy and detachment kinetic at the step edges. DFT calculations also reveal that Pd atoms contribute predominately to the tunneling current in agreement with the STM

results. All the observed surfaces contain Zn and Pd in or near the surface. The higher bond strength between Zn and Pd atoms compared to Pd-Pd or Zn-Zn bonds is suggested as a factor for the stability of selective surfaces. The formation of intermetallics at surfaces may result in ZnPd exhibiting enhanced catalyst properties compared to Zn or Pd elemental counterparts.

ACKNOWLEDGMENTS

This work was performed as a part of the Network for Intermetallic Compounds as Catalysts for Steam Reforming of Methanol, an action of the European Co-operation in Science and Technology (COST Action CM0904) research framework. The ZnPd sample was synthesized in Chemnitz University of Technology, Germany. DFT calculations and experimental works of STM, SEM, EBSD, and optical microscopy were performed at The University of Liverpool, UK. XPS and some of STM measurements were carried out in Institut Jean Lamour, Nancy, France. LEEM/PEEM and μ-LEED were taken in Diamond Light Source, UK, and the Center for Functional Nanomaterials and the National Synchrotron Light Source II, U.S. Department of Energy (DOE) Office of Science facilities at Brookhaven National Laboratory, under Contract No. DE-SC0012704. M. Lowe would like to acknowledge support from the EPSRC Doctoral Training Grant. M. Armbrüster is grateful for the support by the Deutsche Forschungsgemeinschaft (grant AR617/23-1). Cooperation was fostered by the European Integrated Center for the Development of New Metallic Alloys and Compounds (https://www.ecmetac.eu/).

---

[1] M. Armbrüster, M. Behrens, K. Föttinger, M. Friedrich, É. Gaudry, S. K. Matam, and H. R. Sharma. The intermetallic compound ZnPd and its role in methanol steam reforming. *Catalysis Reviews*, 55(3):289–367, 2013.

[2] N. Iwasa, T. Mayanagi, N. Ogawa, K. Sakata, and N. Takezawa. New catalytic functions of Pd-Zn, Pd-Ga, Pd-In, Pt-Zn, Pt-Ga and Pt-In alloys in the conversions of methanol. *Catalysis Letters*, 54(3):119–123, 1998.

[3] N. Iwasa, S. Masuda, N. Ogawa, and N. Takezawa. Steam reforming of methanol over Pd/ZnO: Effect of the formation of PdZn alloys upon the reaction. *Applied Catalysis A, General*,

125(1):145–157, 1995.

[4] M. Krajčí and J. Hafner. Intermetallic compounds as selective heterogeneous catalysts: Insights from DFT. *ChemCatChem*, 8:34–48, 2016.

[5] S. Sá, H. Silva, L. Brandão, J. M. Sousa, and A. Mendes. Catalysts for methanol steam reforming-a review. *Applied Catalysis B: Environmental*, 99(1-2):43–57, 2010.

[6] R. C. Castellano, Y. Liu, A. Moini, G. S. Koermer, and R. J. Farrauto. *US7*, 569:511, 2009.

[7] J. Hu, Y. Wang, D. VanderWiel, C. Chin, D. Palo, R. Rozmiarek, R. Dagle, J. Cao, J. Holladay, and E. Baker. Fuel processing for portable power applications. *Chemical Engineering Journal*, 93(1):55–60, 2003.

[8] A. Casanovas, J. Llorca, N. Homs, J. L. G. Fierro, and P. Ramírez de la Piscina. Ethanol reforming processes over zno-supported palladium catalysts: Effect of alloy formation. *Journal of Molecular Catalysis A: Chemical*, 250(1):44–49, 2006.

[9] V. Engels, A. Rachamim, S. H. Dalal, S. M. L. Pfaendler, J. Geng, A. Berenguer-Murcia, A. J. Flewitt, and A. E. H. Wheatley. Nanoparticulate PdZn as a novel catalyst for ZnO nanowire growth. *Nanoscale Res. Lett.*, 5:904–907, 2010.

[10] X. Cheng, Z. Shi, N. Glass, L. Zhang, J. Zhang, D. Song, Z.-S. Liu, H. Wang, and J. Shen. A review of pem hydrogen fuel cell contamination: Impacts, mechanisms, and mitigation. *J. Power Sour.*, 165:4739–756, 2007.

[11] K. Narusawa, M. Hayashida, Y. Kamiya, H. Roppongi, D. Kurashima, and K. Wakabayashi. Deterioration in fuel cell performance resulting from hydrogen fuel containing impurities: poisoning effects by CO, CH_4, HCHO and HCOOH. *JSAE Rev.*, 24:41–46, 2003.

[12] J. D. Holladay, Y. Wang, and E. Jones. Review of developments in portable hydrogen production using microreactor technology. *Chem. Rev.*, 104:4767–4790, 2004.

[13] H. Purnama, F. Girgsdies, T. Ressler, J. H. Schattka, R. A. Caruso, R. Schomäcker, and R. Schlögl. Activity and selectivity of a nanostructured CuO/ZrO_2 catalyst in the steam reforming of methanol. *Catal. Lett.*, 94:61–68, 2004.

[14] J. P. Shen and C. Song. Influence of preparation method on performance of Cu/Zn-based catalysts for low-temperature steam reforming and oxidative steam reforming of methanol for H_2 production for fuel cells. *Catalysis Today*, 77(1):89–98, 2002.

[15] H. Purnama, T. Ressler, R. E. Jentoft, H. Soerijanto, R. Schlögl, and R. Schomäcker. Co formation/selectivity for steam reforming of methanol with a commercial $CuO/ZnO/Al_2O_3$

catalyst. *Applied Catalysis A: General*, 259(1):83–94, 2004.

[16] N. Takezawa and N. Iwasa. Steam reforming and dehydrogenation of methanol: Difference in the catalytic functions of copper and group VIII metals. *Catalysis Today*, 36(1):45–56, 1997. cited By (since 1996) 181.

[17] M. Friedrich, S. Penner, M. Heggen, and M. Armbrüster. High CO_2 selectivity in methanol steam reforming through ZnPd/ZnO teamwork. *Angewandte Chemie International Edition*, 52(16):4389–4392, 2013.

[18] N. Köwitsch, L. Thoni, B. Klemmed, A. Benad, P. Paciok, M. Heggen, I. Köwitsch, M. Mehring, A. Eychmüller, and M. Armbrüster. Proving a paradigm in methanol steam reforming: Catalytically highly selective In_xPd_y/In_2O_3 interfaces. *ACS Catalysis*, 11(1):304–312, 2021.

[19] H. Lorenz, C. Rameshan, T. Bielz, N. Memmel, W. Stadlmayr, L. Mayr, Q. Zhao, S. Soisuwan, B. Klötzer, and S. Penner. From oxide-supported palladium to intermetallic palladium phases: Consequences for methanol steam reforming. *ChemCatChem*, 5(6):1273–1285, 2013.

[20] Dennis C. A. Ivarsson, Ioannis G. Aviziotis, Toni Keilhauer, and Marc Armbrüster. Fixed-bed reactor for catalytic studies on low-surface area materials. *Review of Scientific Instruments*, 90(1):014101, 01 2019.

[21] W. Stadlmayr, S. Penner, B. Klötzer, and N. Memmel. Growth, thermal stability and structure of ultrathin Zn-layers on Pd(111). *Surface Science*, 603(1):251–255, 2009.

[22] W. Stadlmayr, B. Kratzer, S. Penner, and N. Memmel. Growth and alloying of ultra-thin Zn layers on Pd(110). *The Journal of Physical Chemistry C*, 116(5):3635–3644, 2012.

[23] W. Stadlmayr, Ch. Rameshan, Ch. Weilach, H. Lorenz, M. Hävecker, R. Blume, T. Rocha, D. Teschner, A. Knop-Gericke, D. Zemlyanov, S. Penner, R. Schlögl, G. Rupprechter, B. Klötzer, and N. Memmel. Temperature-induced modifications of PdZn layers on Pd(111). *Journal of Physical Chemistry C*, 114(24):10850–10856, 2010.

[24] Z. X. Chen, K. M. Neyman, and N. Rösch. Theoretical study of segregation of Zn and Pd in Pd–Zn alloys. *Surface Science*, 548(1–3):291–300, 2004.

[25] S. Alarcón Villaseca, D. Kandaskalov, É. Gaudry, and M. Armbrüster. Chemical bonding in zinc-based intermetallic compounds with the CuTi or the CsCl type of structure. *Zeitschrift für Anorganische und Allgemeine Chemie*, 640(5):753–759, 2014.

[26] A. P. Tsai, S. Kameoka, and Y. Ishii. PdZn = Cu: Can an intermetallic compound replace an element? *Journal of the Physical Society of Japan*, 73(12):3270–3273, 2004.

[27] K. Nozawa, N. Endo, S. Kameoka, A. P. Tsai, and Y. Ishii. Catalytic properties dominated by electronic structures in PdZn, NiZn, and PtZn intermetallic compounds. *Journal of the Physical Society of Japan*, 80(6), 2011.

[28] M. Friedrich, D. Teschner, A. Knop-Gericke, and M. Armbrüster. Surface and subsurface dynamics of the intermetallic compound ZnNi in methanol steam reforming. *The Journal of Physical Chemistry C*, 116(28):14930–14935, 2012.

[29] C. Rameshan, W. Stadlmayr, C. Weilach, S. Penner, H. Lorenz, M. Hävecker, R. Blume, T. Rocha, D. Teschner, A. Knop-Gericke, R. Schlögl, N. Memmel, D. Zemlyanov, G. Rupprechter, and B. Klötzer. Subsurface-controlled CO_2 selectivity of PdZn near-surface alloys in H_2 generation by methanol steam reforming. *Angewandte Chemie - International Edition*, 49(18):3224–3227, 2010.

[30] E. Jeroro and J. M. Vohs. Exploring the role of Zn in PdZn reforming catalysts: Adsorption and reaction of ethanol and acetaldehyde on two-dimensional PdZn alloys. *Journal of Physical Chemistry C*, 113(4):1486–1494, 2009.

[31] D. C. A. Ivarsson, U. Burkhardt, K. W. Richter, R. Kriegel, L. Rößner, M. Neumann, and M. Armbrüster. Simple vapor-solid synthesis of zn-based intermetallic compounds. *Journal of Alloys and Compounds*, 743:155–162, 2018.

[32] D. C. A. Ivarsson, U. Burkhardt, M. Heggen, A. Ormeci, and M. Armbrüster. On the twinning in ZnPd. *Physical Chemistry Chemical Physics*, 19:5778–5785, 2017.

[33] B. Delley. An all-electron numerical method for solving the local density functional for polyatomic molecules. *The Journal of Chemical Physics*, 92(1):508–517, 1990.

[34] B. Delley. From molecules to solids with the DMol3 approach. *The Journal of Chemical Physics*, 113(18):7756–7764, 2000.

[35] J. P. Perdew, K. Burke, and M. Ernzerhof. Generalized gradient approximation made simple. *Phys. Rev. Lett.*, 77:3865–3868, 1996.

[36] S. Grimme. Semiempirical GGA-type density functional constructed with a long-range dispersion correction. *Journal of Computational Chemistry*, 27(15):1787–1799.

[37] D. D. Koelling and B. N. Harmon. A technique for relativistic spin-polarised calculations. *Journal of Physics C: Solid State Physics*, 10(16):3107–3114, aug 1977.

[38] M. Douglas and N. M. Kroll. Quantum electrodynamical corrections to the fine structure of helium. *Annals of Physics*, 82(1):89–155, 1974.

[39] B. Delley. Hardness conserving semilocal pseudopotentials. *Phys. Rev. B*, 66:155125, Oct 2002.

[40] B. Hammer, L. B. Hansen, and J. K. Nørskov. Improved adsorption energetics within density-functional theory using revised perdew-burke-ernzerhof functionals. *Phys. Rev. B*, 59:7413–7421, 1999.

[41] B. Delley. A scattering theoretic approach to scalar relativistic corrections on bonding. *International Journal of Quantum Chemistry*, 69(3):423–433, 1998.

[42] B. Delley. Ground-state enthalpies: evaluation of electronic structure approaches with emphasis on the density functional method. *The Journal of Physical Chemistry A*, 110(50):13632–13639, 2006. PMID: 17165892.

[43] C. D. Yuen, B. Unal, D. Jing, and P. A. Thiel. Weak bonding of Zn in an Al-based approximant based on surface measurements. *Philosophical Magazine*, 91(19-21):2879–2888, 2011.

[44] M. Friedrich, D. Teschner, A. Knop-Gericke, and M. Armbrüster. Influence of bulk composition of the intermetallic compound ZnPd on surface composition and methanol steam reforming properties. *Journal of Catalysis*, 285(1):41–47, 2012.

[45] K. S. Kim, A. F. Gossmann, and N. Winograd. X-ray photoelectron spectroscopic studies of palladium oxides and the palladium-oxygen electrode. *Analytical Chemistry*, 46(2):197–200, 1974.

[46] C. J. Powell. Recommended auger parameters for 42 elemental solids. *Journal of Electron Spectroscopy and Related Phenomena*, 185(1–2):1–3, 2012.

[47] A. Lebugle, U. Axelsson, R. Nyholm, and N. Mårtensson. Experimental L and M core level binding energies for the metals 22 Ti to 30 Zn. *Physica Scripta*, 23(5A):825, 1981.

[48] J. C. Klein and D. M. Hercules. Surface characterization of model urushibara catalysts. *Journal of Catalysis*, 82(2):424–441, 1983.

[49] S. Kou and Y. A. Chang. Thermodynamics of ordered β1-PdZn alloys. *Acta Metallurgica*, 23(10):1185–1190, 1975.

[50] H. Gabasch, A. Knop-Gericke, R. Schlögl, S. Penner, B. Jenewein, K. Hayek, and B. Klötzer. Zn adsorption on Pd(111): ZnO and PdZn alloy formation. *Journal of Physical Chemistry B*, 110(23):11391–11398, 2006.

[51] G. Weirum, M. Kratzer, H. P. Koch, A. Tamtogl, J. Killmann, I. Bako, A. Winkler, S. Surnev, F. P. Netzer, and R. Schennach. Growth and desorption kinetics of ultrathin Zn layers on Pd(111). *Journal of Physical Chemistry C*, 113(22):9788–9796, 2009.

[52] H. P. Koch, I. Bako, G. Weirum, M. Kratzer, and R. Schennach. A theoretical study of Zn adsorption and desorption on a Pd(111) substrate. *Surface Science*, 604(11):926–931, 2010.

[53] H. Zhou, X. Yang, L. Li, X. Liu, Y. Huang, X. Pan, A. Wang, J. Li, and T. Zhang. PdZn intermetallic nanostructure with Pd–Zn–Pd ensembles for highly active and chemoselective semi-hydrogenation of acetylene. *Acs Catalysis*, 6(2):1054–1061, 2016.

[54] H. Yoshida, T. Zama, S. Fujita, J. Panpranot, and M. Arai. Liquid phase hydrogenation of phenylacetylene over Pd and PdZn catalysts in toluene: Effects of alloying and CO_2 pressurization. *RSC Advances*, 4(47):24922–24928, 2014.

[55] T. Gunji, H. Ochiai, T. Ohira, Y. Liu, Y. Nakajima, and F. Matsumoto. Preparation of various Pd-based alloys for electrocatalytic CO_2 reduction reaction—selectivity depending on secondary elements. *Chemistry of Materials*, 32(16):6855–6863, 2020.

[56] K. M. Naik, K. Hashisake, T. Hamada, E. Higuchi, and H. Inoue. Intermetallic PdZn nanoparticles loaded on deficient TiO_2 nanosheets as a support: a bifunctional electrocatalyst for oxygen reduction in PEMFCs and the glycerol oxidation reactions. *Journal of Materials Chemistry A*, 10(26):13987–13997, 2022.

[57] Y. Qiu, J. Zhang, J. Jin, J. Sun, H. Tang, Q. Chen, Z. Zhang, W. Sun, G. Meng, Q. Xu, Z. Youqi, A. Han, L. Gu, D. Wang, and Y. Li. Construction of Pd-Zn dual sites to enhance the performance for ethanol electro-oxidation reaction. *Nature Communications*, 12(1):5273, 2021.

[58] M. Ma, X. Han, H. Li, X. Zhang, Z. Zheng, L. Zhou, J. Zheng, Z. Xie, Q. Kuang, and L. Zheng. Tuning electronic structure of PdZn nanocatalyst via acid-etching strategy for highly selective and stable electrolytic nitrogen fixation under ambient conditions. *Applied Catalysis B: Environmental*, 265:118568, 2020.

[59] T. Hirano. *A Note on Thermochemistry, in MOPAC Manual*. 7 edition, 1993.

SUPPLEMENTARY MATERIALS

For calculation of thermodynamic energies and kinetics, the $DMol^3$ package is employed in the commercial DFT Electronic Structure Program, Biovia Materials Studio [33, 34]. DFTD (Generalized Gradient Approximation (GGA) + dispersion correction) calculations were carried out using the GGA functional within the Perdew-Burke-Ernzerhof (PBE) framework [35] and the dispersion correction method of Grimme [36]. The relativistic corrections [37, 38] were employed using DSPP (DFT-Semicore Pseudopotential) [39].

As outlined in the main text, STM simulation was conducted using the CASTEP module. Prior to the STM simulation, geometry optimization was performed again with the function that was used for STM simulation in CASTEP. Calculations were done using a revised Perdew-Burke-Ernzerhof (PBE) [35] GGA functional, RPBE [40], and relativistic correction using the VPSR pseudopotential [41].

All the input files used in the final step of DFT calculation for Energy, Geometry Optimization and STM simulation are generated employing the commercial windows version of MS Studio platforms, and structural models are generated/sketched using Visualizer modules by selecting the default fine setting or custom setting better than default fine setting. Custom settings are as follows: Spin is set unrestricted, Electron occupation smearing is set 0.1 eV in CASTEP and 0.003 Hartree in $DMol^3$, K-point spacing is used about 0.04/Å but better than 0.05/Å, energy convergence per atom 1×10^{-6} in $Dmol^3$ and 5×10^{-7} in the CASTEP, Orbital cutoff in $DeMol^3$ is 4.5 Å, plane wave basis set cut-off in CASTEP is 350 eV.

Before surface energy calculation and STM simulation, the ZnPd bulk unit cells were constructed in face-centered tetragonal (FCT) representation, and geometry was optimized. Then the bulk supercells were formed by redefining lattice vectors to have a plane parallel to a surface of interest having at least 6 or 8 atomic layers. Surfaces having vacuum slabs $\sim$ 10 Å or larger were made from the supercell of the bulk supercell. Actual slab thickness was chosen to maintain identical k-spacing in the bulk and surface structure in a set. Then the primitive unit cells were obtained from the 6 or 8 layers considering the symmetry of 2D lattice.

The surface atomic layers were relaxed for primitive unit cells with the vacuum slabs. The DFT energy of the surface was then calculated from the difference in the total energy

of the primitive lattice with the vacuum slab and the corresponding bulk supercell.

In order to calculate the thermodynamic energies, and the detachment kinetics at the step, steps are formed at the top surface layer parallel to the low index surface of ZnPd. Superlattices were formed such that Hessian atoms (Pd, Zn or ZnPd pair of interest) are separated larger than the orbital cut-off considered in DFT calculation.

First-order force constants K_{ijxx}, K_{ijxy}, K_{ijxz}, K_{ijyx}, K_{ijyy}, K_{ijyz}, K_{ijzx}, K_{ijzy}, K_{ijzz}, were obtained from the DFT-calculated forces K_{js} were considered finite for all surface atoms within 5 Å of any surface atom i, and all other K_{js} zero. Then the normal modes of vibration of Hessian atoms were computed. Hessian atoms here are defined as the atoms of interest for which we displace them from their equilibrium positions and calculate the first-order force constants for all atoms in a large supercell.

Vibrational energies and thermodynamic free energies versus temperatures were computed by

$$E_{vib} = \sum_i \left(\frac{1}{2} + \langle n \rangle_i \right) h\nu_i,$$

with $n = 0, 1, 2, \ldots \infty$, and the expectation value $\langle n \rangle_i$ or statistical weight at a temperature T can be found by considering the Bose-Einstein distribution as

$$\langle n \rangle = \sum_i \langle n \rangle_i = \sum_i \frac{e^{-\frac{h\nu_i}{k_B T}}}{1 - e^{-\frac{h\nu_i}{k_B T}}}$$

Vibrational enthalpy per model structure is thus [59],

$$E_{vib} = \frac{1}{2} \sum_i h\nu_i + \sum_i \frac{h\nu_i e^{-\frac{h\nu_i}{k_B T}}}{1 - e^{-\frac{h\nu_i}{k_B T}}}$$

And vibrational entropy per model structure [59],

$$S_{vib} = \sum_i \frac{(h\nu_i/T) e^{-\frac{h\nu_i}{k_B T}}}{1 - e^{-\frac{h\nu_i}{k_B T}}} - k \sum_i [1 - e^{-\frac{h\nu_i}{k_B T}}].$$

Surface free energy at a temperature is obtained, then, by adding the vibrational contribution, $\Delta E_{vib} - T\Delta S_{vib}$, to the DFT electronic surface energies, $E = E_{DFT} + \Delta E_{vib} - T\Delta S_{vib}$.

To compute the competition of kinetic detachment, detachment barriers were considered as the DFT bond energy of an atom or a pair of atoms (ZnPd) at the surface with the bulk. Attempt frequency, $\langle \nu \rangle$, for a particular kinetic process (activation against energy barrier)

was considered as the temperature-dependent weighted vibrational frequency at surfaces for that particular process:

$$\overline{\nu} = \sum_{j} \sum_{i} \frac{(h\nu_i/T)e^{-\frac{h\nu_i}{k_B T}}}{1 - e^{-\frac{h\nu_i}{k_B T}}}$$

The probability of detachment is computed as:

$$\frac{P}{A} = \nu e^{-\frac{E_{DFT}}{k_B T}}$$